Chemical Science

ROYAL SOCIETY OF CHEMISTRY

EDGE ARTICLE

View Article Online
View Journal | View Issue

Cite this: *Chem. Sci.*, 2025, **16**, 13855

All publication charges for this article have been paid for by the Royal Society of Chemistry

Tailoring the local acid-like microenvironment with the synergism of nanoscale and atomically local electric fields for enhanced hydrogen spillover in alkaline seawater electrolysis†

Lei Jin, Zhiyuan Wang, Hui Xu, * Kun Wang, Xingyue Qian, Haiqun Chen * and Guangyu He*

Creating an environment with a high concentration of acidic protons in the absence of a Lewis acid layer is challenging for alkaline seawater hydrogen spillover (HSo). Herein, we introduce a synergistic strategy by creating both nanoscale and atomically local electric fields to generate a local high-concentration acid-like environment. This is demonstrated by incorporating multiple atomically dispersed Ru nanoparticles (Ru NPs) on the surface of Co_xPv@C. Finite element method (FEM) simulations and advanced characterizations illustrate that the nanoscale and atomically local electric fields promote the formation of a significant number of H_3O^+, creating a local acid-like environment around the surface of multiple Ru NPs. The small work function difference ($\Delta\Phi$) of 0.05 eV between Ru and Co_xP@C is found to be favorable for interfacial HSo. *In situ* Raman spectroscopy confirms that the formed P–H bond acts as a proton "sponge", storing H^+ and quickly transferring them to the Ru NPs surface, where they combine with adjacent H_2O molecules to form H_3O^+, thus promoting HSo. Additionally, the carbon layer and the inherent corrosion resistance of Co_xPv@C can effectively protect the Ru NPs from the toxicity and corrosion caused by Cl^-. Consequently, the Ru-Co_xPv@C catalyst exhibits long-term stability for 200 h at 10 mA cm^2 in alkaline seawater electrolyte.

Received 25th March 2025
Accepted 23rd June 2025

DOI: 10.1039/d5sc02290h

rsc.li/chemical-science

1. Introduction

Hydrogen (H_2) is a crucial energy carrier and a key raw material for producing important chemicals such as ethanol and ammonia.[1,2] However, its production process still largely depends on energy-intensive fossil fuels, a method referred to as grey/blue H_2 production.[3,4] Electrolyzing seawater for large-scale production of H_2 is expected to reduce the utilization of fresh water.[5–7] However, H_2 production from direct seawater splitting is technically challenging because the high levels of dissolved ions (Ca^{2+}, Mg^{2+}, K^+, Cl^-, Br^-, SO_4^{2-}, *etc.*) in seawater can trigger deactivation of catalysts and damage equipment (electrodes, cells, membranes, *etc.*).[8–10] Moreover, compared with hydrogen production in acidic environments, the hydrogen evolution reaction (HER) kinetics in alkaline environments are at least two orders of magnitude slower, primarily due to the slower rate of water dissociation.[11–14] Furthermore, alkaline seawater typically demands more energy for the dissociation of H_2O to generate H^+ due to the inherently proton-deficient environment.[15,16] Therefore, these complex environments may degrade the HER performance.

To eliminate these practical challenges, in addition to eliminating the attack by Cl^- in alkaline seawater, it is essential to overcome the limitations associated with proton formation and evolution during the alkaline HER. To date, however, most reported investigations have focused on repelling the Cl^- by *in situ* self-transformation into anion layers or adding additional anions to the catalyst's surface to form passivating layers.[17–20] These strategies are likely to be unsustainable during adsorption of passivating anion layers and effective repulsion of the Cl^- on active sites. Therefore, it is necessary to leverage the inherent properties of catalysts to enhance their resistance to corrosion and impurities. Moreover, such an alkaline environment lacks a proton supply environment, which is an obstacle to the cathodic HER.[21–23] It was reported that adjusting the local environment at the catalyst surface allows alkaline seawater electrolysis. Based on this, it is hypothesized that the creation of a local acid-like environment on a catalyst surface can promote hydrogen species accumulation and migration to achieve acid-like HER performance. So far, this local environment has mainly been achieved by introducing a Lewis acid layer (for instance, MgO, V_2O_3, Cr_2O_3, WO_2 and MnO_2) on a catalyst

Key Laboratory of Advanced Catalytic Materials and Technology, Advanced Catalysis and Green Manufacturing Collaborative Innovation Center, Changzhou University, Changzhou, Jiangsu Province 213164, China. E-mail: xuhui006@cczu.edu.cn; chenhq@cczu.edu.cn; hegy@cczu.edu.cn

† Electronic supplementary information (ESI) available. See DOI: https://doi.org/10.1039/d5sc02290h

surface to dynamically split water molecules and capture hydroxyl anions.[24–29] However, this single approach is insufficient for creating an environment with a high concentration of local acidic protons, and generating this high-concentration local environment in the absence of a Lewis acid layer in alkaline seawater conduction is extremely challenging.

Here, we introduce a coupling strategy to create nanoscale and atomically local electric fields by incorporating atomically dispersed high-curvature Ru nanoparticles (Ru NPs) on the surface of Co_xPv@C. This approach focuses on enriching the proton concentration of the local acid-like environment and simultaneously accelerating H* desorption. Finite element method (FEM) simulations and related characterizations illustrate that the nanoscale and atomically local electric fields promote the formation of a significant number of H_3O^+, creating a local acid-like environment around the surface of multiple Ru NPs. The small work function difference ($\Delta\Phi$) of 0.05 eV between Ru and Co_xP is found to be favorable for interfacial hydrogen spillover (HSo). *In situ* Raman spectroscopy demonstrates that the formed P–H acts as a proton "sponge", stores H^+, then quickly transfers the H^+ to the surface of the Ru NPs, which subsequently combines with adjacent H_2O molecules to form H_3O^+ and promotes HSo. Moreover, the carbon layer and the inherent corrosion resistance of Co_xPv@C effectively protect the Ru NPs from the toxicity and corrosion caused by Cl^-. Consequently, the Ru-Co_xPv@C catalyst exhibits long-term stability for 200 h at 10 mA cm^2 in alkaline seawater electrolyte.

2. Experimental section

2.1 Synthesis of Ru-Co(OH)$_2$

First, 0.291 g of $Co(NO_3)_2\cdot 6H_2O$, a certain amount of $RuCl_3\cdot H_2O$ and 0.567 g of hexamethylenetetramine were weighed and completely dissolved in a Teflon autoclave with 50 mL of ethanol, then stirred for 2 h. After reaction for 10 h at 120 °C, the brown Ru-$Co(OH)_2$ precipitate was collected *via* centrifugation with ethanol and dried at 60 °C overnight.

2.2 Synthesis of Ru-Co_xPv@C

The as-prepared Ru-$Co(OH)_2$ precursor and 0.5 g of $NaH_2PO_2\cdot H_2O$ were placed in two separate positions in a ceramic boat inside a tube furnace, with $NaH_2PO_2\cdot H_2O$ positioned upstream of the gas flow and Ru-$Co(OH)_2$ placed downstream. The temperature was then gradually increased to 350 °C, where it was maintained for 2 h. After cooling to room temperature, a round nanoparticle-aggregated nano-microsphere morphology of Ru was obtained on the surface of Co_xPv@C.

2.3 Material characterization and electrochemical methods

The material characterization and electrochemical methods are documented in the ESI† in detail.

3. Results and discussion

3.1 Material synthesis and characterization

The Ru-Co_xPv@C was prepared through a two-step process involving a solvothermal reaction followed by phosphorization treatment. As illustrated in Fig. 1a, the Ru nanoparticles anchored on the Co_xPv@C surface create a local acid-like environment, while the carbon layer and the inherent corrosion resistance of Co_xPv@C effectively protect the Ru region from Cl^--induced toxicity and corrosion, thereby achieving excellent HER performance. The morphology was characterized using scanning electron microscopy (SEM) to provide detailed structural information. The Ru-$Co(OH)_2$ shows a rough nanoparticle-aggregated-like morphology. After phosphorization treatment, the Ru nanoparticle-aggregated nano-microspheres can be clearly observed anchored on the Co_xPv@C surface (Fig. 1b and S1†). This high-curvature morphology, resembling a nanopyramid, facilitates electron accumulation at the tip region, generating a strong local electric field at the nanoscale. The concentration of electrons subsequently activates a locally acidic proton-rich environment, promoting the alkaline HSo effect.[30] To validate this hypothesis, we employed the FEM to investigate the potential of tip-enhanced nanoscale field amplification (Fig. 1c and d). It was observed that the electron density at the sharpest point of the high-curvature structure increases significantly, resulting in the formation of a strong local nanoscale electric field. This phenomenon can be attributed to the electric field between charges, where free electrons migrate to the sharpest Ru

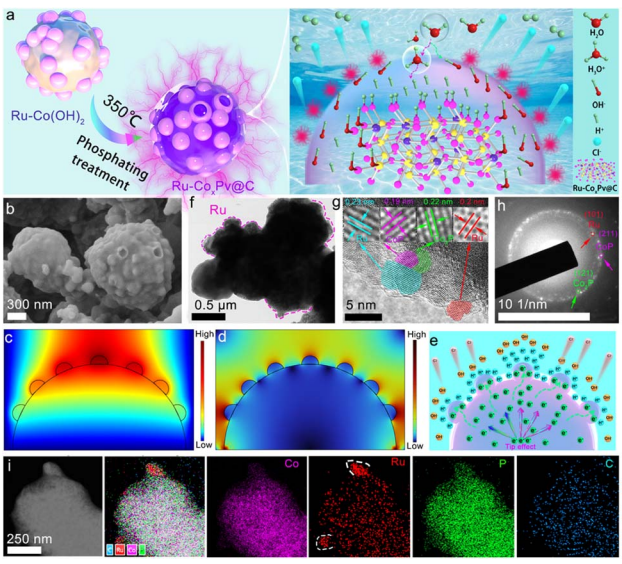

Fig. 1 (a) Schematic illustration of the formation of Ru-Co_xPv@C and the functionalization process. (b) SEM image of Ru-Co_xPv@C. (c and d) Simulated electron distribution and electric field intensity around the surface of the high-curvature nanoparticles. (e) Schematic illustration showing the influence of the high-curvature nanotip electric field on cation aggregation. (f) TEM image (pink marks represent Ru NPs) and (g) high-resolution TEM image of Ru-Co_xPv@C. (h) SAED pattern for Ru-Co_xPv@C. (i) Mapping images of Ru-Co_xPv@C (white marks represent Ru element distribution).

nanoparticle regions during the electrochemical reaction, which promotes the production of abundant H_3O^+ around the Ru tip region and forms a local micro-acidic environment for hydrogen overflow under alkaline conditions (Fig. 1e). Transmission electron microscopy (TEM) was applied to gain more detailed insights into the structural characteristics of the Ru-Co_xPv@C. The round Ru nanoparticles exhibit an average length of 150 nm (Fig. 1f). As illustrated in the high-resolution TEM (HRTEM) image (Fig. 1g), the lattice fringes with approximate spacing of 0.23 and 0.2 nm are assigned to the (100) and (101) crystal planes of Ru nanoparticles, while the lattice fringes with approximate spacing of 0.19 and 0.22 nm are assigned to the (211) and (121) crystal planes of CoP and Co_2P in the Ru-Co_xPv@C sample, respectively. In the selected area electron diffraction pattern (SAED, Fig. 1h), the CoP (211) plane, Co_2P (121) plane and Ru (101) plane are clearly distinguishable in the Ru-Co_xPv@C structure. Elemental mapping further corroborates the successful incorporation of Ru NPs, where the distributions of Ru, Co, P and C elements are relatively uniform, verifying the successful preparation of the Ru-Co_xPv@C structure (Fig. 1i). The ICP test confirmed the content of Ru element is 3.8 wt% (38 g kg^{-1}) in the Ru-Co_xPv@C structure, which is close to that of 2.18 wt% obtained in the STEM-EDS mapping test (Fig. S2†). Notably, the Ru element is mainly distributed in the tip region (white dotted oval frame).

X-ray diffraction (XRD) analysis was initially performed to assess whether the incorporation of Ru atoms influences the crystal phase of the catalyst. As depicted in Fig. S3,† four distinct peaks are observed at around 19.1°, 32.5°, 37.9° and 51.6° attributed to the (001), (100), (101) and (102) crystal planes of $Co(OH)_2$ (JCPDS No. 30-0443), repsectively.[31] Notably, the broadening and shifting of the peaks is ascribed to the incorporation of Ru atoms. For the Ru-Co_xPv@C structure (Fig. 2a), the peaks located at 31.6°, 36.3°, 48.1°, and 56.8° belong to the (011), (111), (211), and (301) crystal planes of CoP (JCPDS No. 29-0497), respectively, whereas the peaks at 40.8°, 41.0° and 43.3° are correlated to the (121), (201), and (211) crystal planes of Co_2P (JCPDS No. 32-0306), respectively, and the characteristic peak of Ru is scarcely detectable, likely due to the low concentration of Ru atoms embedded within the Co_xPv structure.[32,33] Moreover, the Fourier transform infrared (FT-IR) spectra were recorded to investigate the presence of different functional groups. The absorption peak at 3465 cm^{-1} depicted in Fig. 2b is ascribed to the O–H stretching vibration in $Co(OH)_2$, while the peaks in the lower wavelength range (500–1000 cm^{-1}) are attributed to Co–O and Co–O–Co lattice vibrations. In the case of Ru-Co_xPv@C, the peaks at approximately 918 and 1076 cm^{-1} are associated with the P–M and P–O stretching vibrations, respectively.[34,35] XRD and FT-IR analyses indicate the successful synthesis of Ru–$Co(OH)_2$ and Ru-Co_xPv@C. To investigate the impact of $Co(OH)_2$ and Co_xP on the modification of Ru's electronic structure, electron paramagnetic resonance (EPR) spectra of Ru–$Co(OH)_2$ and Ru-Co_xPv@C were recorded. As illustrated in Fig. 2c, compared to the case of Ru embedded in $Co(OH)_2$ with oxygen vacancies, in Ru supported on phosphorus vacancy-rich Co_xPv, significant electron transfer occurs from the phosphorus vacancies—populated with numerous unpaired

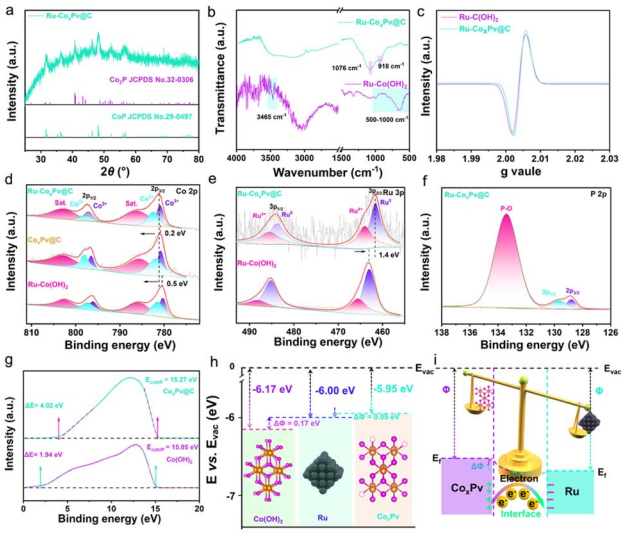

Fig. 2 (a) XRD pattern for Ru-Co_xPv@C. (b) FT-IR spectra for Ru-$Co(OH)_2$ and Ru-Co_xPv@C. (c) EPR spectra for Ru-$Co(OH)_2$ and Ru-Co_xPv@C. (d) High-resolution Co 2p spectra for Ru-$Co(OH)_2$, Co_xP and Ru-Co_xPv@C, (e) Ru 3p XPS spectra for Ru-$Co(OH)_2$ and Ru-Co_xPv@C and (f) P 2p XPS spectra for Ru-Co_xPv@C. (g) UPS spectra for $Co(OH)_2$, Co_xPv and Ru. (h) Energy-band alignment diagram of $Co(OH)_2$ and Co_xPv with respect to Ru. (i) Interfacial electronic configurations for HSo during the HER.

electrons—to the Ru nanoparticles, resulting in the formation of electron-enriched Ru regions ($Ru^{\delta-}$).[25] Accordingly, X-ray photoelectron spectroscopy (XPS) was subsequently utilized to analyze the chemical composition and bonding configuration of Ru-$Co(OH)_2$ and Ru-Co_xPv@C. In the high-resolution Co 2p spectrum for Ru-Co_xPv@C (Fig. 2d), two prominent peak doublets observed at 780.9 and 797.1 eV and 782.4 and 797.9 eV are attributed to the Co^{3+} and Co^{2+} components, respectively, while the peaks at 786.2 eV and 802.7 eV are attributed to the shake-up satellite peaks. Compared with Co_xPv@C and Ru-$Co(OH)_2$, the Co 2p peak displays a slight positive shift of about 0.2 and 0.5 eV, demonstrating the reduction in charge density around the Co atom. The two pairs of peaks attributed to Ru^0 species (464.0 and 485.5 eV) and $Ru^{\delta+}$ (461.6 and 483.8 eV) are also shown in the high-resolution Ru 3p spectra. In contrast, the binding energy of Ru 3p exhibits a negative shift (~1.4 eV) compared to that of Ru-$Co(OH)_2$, illustrating an increase in the charge density of the Ru atoms (Fig. 2e).[36,37] Meanwhile, for P 2p orbitals, the peaks located at 128.8, 129.7 and 133.4 eV are attributed to the P $2p_{3/2}$, P $2p_{1/2}$ and P–O bonding state in Fig. 2f.[38] These shifts confirm the electron transfers from the Co_xPv interface to the Ru atom to generate the atomically local electric field. Owing to the electrostatic attraction between the negatively charged Ru atoms and the positively charged H_3O^+ species, the Ru nanoparticle region can create a local micro-acid environment for alkaline HSo.[39] Generally, suppressing interfacial charge transfer and minimizing the accumulation of charge at the interface are anticipated to significantly reduce the energy barrier for HSo, thereby theoretically enhancing the catalytic HER performance. This hypothesis is supported by

a comprehensive evaluation and qualitative analysis of the Fermi level (E_f) based on the Φ of the catalysts.[40,41] Ultraviolet photoelectron spectroscopy (UPS) characterization was employed to analyze the Φ values of $Co(OH)_2$ and Co_xP@C, as depicted in Fig. 2g and Table S1.† The measured Φ values for $Co(OH)_2$ and Co_xPv@C are 6.17 and 5.95 eV, and the Φ value for Ru (6.0 eV) is referenced from Wang's work (Fig. 2h).[42] Compared to the relatively larger $\Delta\Phi$ of 0.17 eV between Ru and Co(OH), the Ru-Co_xPv@C interface exhibits a relatively smaller $\Delta\Phi$ of 0.05 eV. $\Delta\Phi$ plays a crucial role in governing the HSo transfer kinetics at the interface. Minimizing $\Delta\Phi$ is theoretically expected to lower the HSo barrier, leading to effective HER performance.[43] In addition, the relative Φ level implies electron overflow from Co_xPv@C to Ru, forming an atomically local electric field, which promotes the production of abundant H_3O^+ around the Ru nanoparticles, thus forming a local micro-acid environment for hydrogen overflow under alkaline conditions.

3.2 Electrocatalytic performance of the HER in alkaline seawater

To experimentally investigate the effect of the modulation of the Φ on the electrocatalytic HSo behavior of the electrodes, linear sweep voltammetry (LSV) was performed using a standard three-electrode system in an alkaline seawater solution. As anticipated, Ru-Co_xPv@C sample exhibits superior electrocatalytic HER performance compared to Ru-$Co(OH)_2$ and Co_xP, $Co(OH)_2$, and it is also better than Pt/C at a large current density. Concretely, small overpotentials of 94 and 240 mV are required to attain η_{10} and η_{50} for HER (Fig. 3a and b), surpassing the performance of Ru-$Co(OH)_2$ (249 and 336 mV) and Co_xP (256 and 382 mV), and the HER activity of $Co(OH)_2$ is almost negligible. The Ru-Co_xPv@C sample also exhibits a lower Tafel slope (137.8 mV dec^{-1}) compared to the referenced samples, indicating its rapid reaction kinetics during the HER (Fig. 3c). Moreover, the electrochemically active surface area (ECSA) was evaluated by determining the double-layer capacitance (C_{dl}) calculated from cyclic voltammetry (CV), providing insight into the surface properties of the samples. Fig. 3d and S4† exhibit that the C_{dl} for Ru-Co_xPv@C is calculated to be 4.7 mF cm^{-2}, larger than that of Ru-$Co(OH)_2$ (4.5 mF cm^{-2}), Co_xP (0.8 mF cm^{-2}) and $Co(OH)_2$ (0.82 mF cm^{-2}), and the estimated ECSA values of Ru-Co_xPv@C, Ru-$Co(OH)_2$, Co_xPv@C, and $Co(OH)_2$ were ~23.1, ~22.1,~4.0 and ~3.9 cm^{-2}, respectively, indicating a larger ECSA. To compare the intrinsic activity of the different catalysts more accurately, the ECSA-normalized LSV curves were plotted (Fig. S5†), and the results show that the intrinsic catalytic activity obeys the following trend: Ru-Co_xPv@C > Ru-$Co(OH)_2$ > $Co(OH)_2$. To further assess the intrinsic HER activity, Fig. 3e, S6 and S7† present the turnover frequency (TOF) values for Ru-Co_xPv@C and the referenced samples. Ru-Co_xPv@C shows a higher TOF value of 4.5 s^{-1} at an overpotential of 300 mV, which is approximately 1.63 times higher than that of Co_xP (2.77 s^{-1}) and about 1.52 times higher than that of Ru-$Co(OH)_2$ (2.95 s^{-1}) at the same overpotential. Subsequently, the HER performances of Ru-Co_xPv@C and Ru-$Co(OH)_2$were measured in different electrolyte; compared with HER activity discrepancy of Ru-$Co(OH)_2$, it was seen that the HER activity of Ru-Co_xPv@C displays hardly any change in tendency with and without Cl^-, indicating that the carbon layer and the inherent corrosion resistance of Co_xP@C effectively protect the Ru region from the toxicity and corrosion of Cl^- (Fig. 3f and S8†).[44,45] Furthermore, the electrochemical stability of Ru-Co_xPv@C was evaluated *via* cyclic voltammetry (CV) testing, and the LSV curve of Ru-Co_xPv@C after 1000 CV cycles closely matches the initial curve, demonstrating its exceptional cyclability (Fig. 3g). Long-term stability was assessed through chronoamperometric measurements, where the electrochemical performance of Ru-Co_xPv@C remained stable over 200/95 h at 10/200 mA cm^{-2} with minimal change. Additionally, the multi-current test, where the current density was varied between 10 and 50 mA cm^{-2} every 1000 s, further confirms the catalyst's high mass transport capability and stability, as evidenced by the immediate potential response at each step, indicating exceptional durability and anti-chloride performance in the Ru-Co_xPv@C sample (Fig. 3h and S9†). SEM and XRD analyses were performed to investigate the structural transformation of Ru-Co_xPv@C after prolonged electrolysis. After the HER test, there was negligible change in the SEM image and XRD pattern for Ru-Co_xPv@C, except that the peak intensity was weaker than that before the test, indicating that the electrode exhibits excellent structural stability (Fig. S10†).

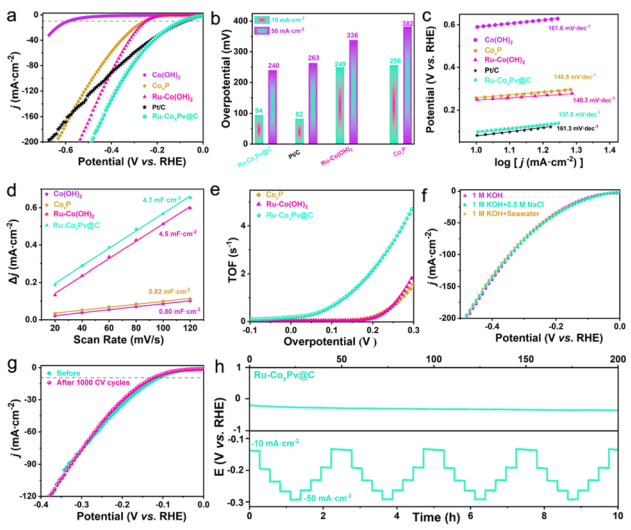

Fig. 3 (a) LSV curves and (b) η_{10} and η_{50} values for Ru-Co_xPv@C and reference samples. (c) Corresponding Tafel plots for Ru-Co_xPv@C and reference samples. (d) C_{dl} values for different catalysts (e) TOF values. (f) LSV for Ru-Co_xPv@C in various solutions. (g) Polarization curves for the HER after 1000 cycles. (h) Chronopotentiometric curves and multi-step chronopotentiometry test results for Ru-Co_xPv@C.

3.3 Acidic HER performance and alkaline overall seawater

The HER catalytic activity of Ru-$Co(OH)_2$ and Ru-Co_xPv@C were also measured in 0.5 M H_2SO_4. Fig. 4a and b reveals a larger HER performance discrepancy (75 mV at η_{10}) for Ru-$Co(OH)_2$ under alkaline and acidic conditions. Conversely, the η_{10} value for Ru-Co_xPv@C (84 mV) displays a slightly decreasing tendency

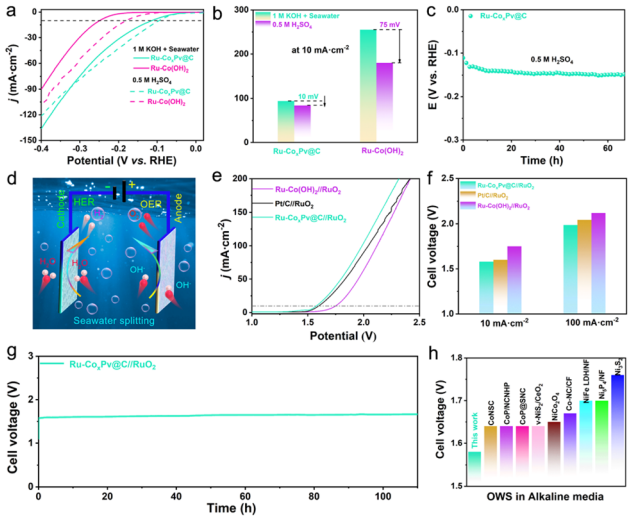

Fig. 4 (a) LSV curves for Ru-Co_xPv@C and Ru-$Co(OH)_2$ in alkaline and acidic solution. (b) Comparison of the HER activity of Ru-Co_xPv@C and Ru-$Co(OH)_2$ under acidic and alkaline conditions. (c) CP curves for Ru-Co_xPv@C in 0.5 M H_2SO_4. (d) The schematic diagram of overall water splitting in the two-electrode configuration. (e) Polarization curves for OWS in alkaline seawater solution. (f) Overpotential of the as-prepared samples at 10 and 100 mA cm^{-2}. (g) CP curve for Ru-Co_xPv@C||RuO_2. (h) Comparison of Ru-Co_xPv@C||RuO_2 with reported overall water splitting electrocatalysts at 10 mA cm^{-2}.

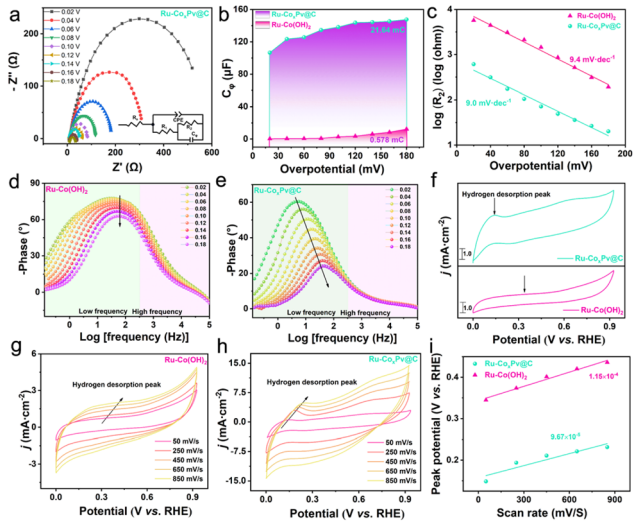

Fig. 5 (a) EIS curves for Ru-Co_xPv@C for the HER in alkaline seawater solution. (b) Plots of C_φ *vs.* overpotential for Ru-$Co(OH)_2$ and Ru-Co_xPv@C during the HER. (c) EIS-derived Tafel plots for the Ru-$Co(OH)_2$ and Ru-Co_xPv@C samples attained from the hydrogen adsorption resistance, R_2. Phase angles for (d) Ru-$Co(OH)_2$ and (e) Ru-Co_xPv@C at different potentials. (f) CV curves for Ru-$Co(OH)_2$ and Ru-Co_xPv@C with a scan rate of 50 mV s^{-1}. (g and h) CV curves for Ru-$Co(OH)_2$ and Ru-Co_xPv@C with different scan rate. (i) Plots of hydrogen desorption peak position *vs.* scan rates for the Ru-$Co(OH)_2$ and Ru-Co_xPv@C samples.

compared with in alkaline seawater solution, suggesting the acid-like HER behavior of Ru-Co_xPv@C in an alkaline medium, and also confirming that a local micro-acid environment is created around the $Ru^{\delta-}$ nanoparticles in Ru-Co_xPv@C in alkaline solution. Moreover, Ru-Co_xPv@C displays good advantages in acidic HER stability (Fig. 4c). To further investigate the hydrogen production capability in a two-electrode system (Fig. 4d), we also evaluated the overall water splitting performance in alkaline seawater solution by using Ru-Co_xPv@C as the cathode and a RuO_2 electrode as the anode. For comparison, the overall water splitting (OWS) performance of Ru-$Co(OH)_2$||RuO_2 and commercial Pt/C||RuO_2 were also measured. The polarization curves in Fig. 4e and f indicate that the required voltage is as low as 1.58 and 1.98 V to drive the η_{10} and η_{100}, respectively, for Ru-Co_xPv@C||RuO_2, superior to those of Pt/C||RuO_2 (1.6 and 2.04 V) and Ru-$Co(OH)_2$||RuO_2 (1.75 and 2.12 V). Remarkably, after continuous operation for over 100 h at η_{10}, it remained stable without evidence of a decline in activity (Fig. 4g). Fig. 4h and Table S2† clearly demonstrate the potential of Ru-Co_xPv@C to rival recent state-of-the-art catalysts in OWS.

3.4 Hydrogen spillover mechanisms

Operando electrochemical impedance spectroscopy (EIS) was measured to probe the adsorption of active hydrogen species (Fig. 5a, S11 and Table S3†). All Nyquist plots were fitted using a double-parallel equivalent circuit model, where R_s corresponds to the uncompensated solution resistance, R_1 denotes the charge transfer resistance associated with H_2O adsorption and activation, and R_2 represents the resistance related to hydrogen adsorption. At any overpotentials, the Ru-Co_xPv@C catalyst exhibits lower values for both R_1 and R_2 compared to Ru-$Co(OH)_2$, indicating more efficient charge transfer between the catalyst surface and H_2O molecules. The hydrogen adsorption charge (Q_H), obtained by integrating the adsorption pseudocapacitance (C_φ) as a function of overpotential (η), is considered a reliable indicator of the quantity of hydrogen adsorbed on the catalyst surface during the HER.[46] The Q_H of Ru-Co_xPv@C (21.64 mC) is approximately 37 times greater than that of Ru-$Co(OH)_2$ (0.578 mC), demonstrating significantly enhanced interfacial HSo from Ru to Co_xPv. This result highlights the role of Co_xPv as an efficient mediator for hydrogen adsorption, providing a straightforward pathway for optimizing the hydrogen adsorption capability (Fig. 5b and Table S3†). Furthermore, plotting $\log R_2$ against the overpotential corresponding to the EIS-derived Tafel slopes enables the quantification of hydrogen adsorption kinetics for Ru-$Co(OH)_2$ and Ru-Co_xPv@C. As illustrated in (Fig. 5c), the smaller slope of 9.0 mV dec^{-1} for Ru-Co_xPv@C indicates significantly accelerated hydrogen adsorption kinetics. The Bode phase plots in Fig. 5d and e reveal that the phase angle decreases as the overpotential shifts from 0.02 to 0.18 V, suggesting that the HER primarily occurs at the low-frequency (LF) interface. In contrast, for Ru-$Co(OH)_2$, the phase angle remains nearly unchanged in the high-frequency (HF) region, indicating a stable electrolyte–electrode interface. Conversely, for Ru-Co_xPv@C, the phase angle in the HF region increases with the applied potential, implying that the electrolyte–electrode interface is dynamic. This variation likely originates from HSo from Co_xP to Ru,

facilitating the formation of Ru–H species.[47] To investigate the hydrogen desorption behavior, *operando* CV measurements were performed on Ru-$Co(OH)_2$ and Ru-Co_xPv@C samples.[48] As shown in Fig. 5f, the oxidation peaks observed within the potential range of 0.20–0.45 V *vs.* RHE are attributed to hydrogen desorption rather than electrochemical surface oxidation of the electrode. The relatively weak hydrogen desorption peak intensity for Ru-$Co(OH)_2$ suggests an absence of significantly enhanced desorbed hydrogen quantities, indicating negligible HSo from Ru-$Co(OH)_2$-to-Ru. Meanwhile, the pronounced hydrogen desorption peak observed for Ru-Co_xPv@C unequivocally confirms the significantly enhanced HSo, which facilitates the accumulation of abundant active hydrogen species at the Ru tip regions. The kinetics of hydrogen desorption was further quantified by plotting the hydrogen desorption peak shift in the CV curves of Ru-$Co(OH)_2$ and Ru-Co_xPv@C as a function of scan rate. Notably, the substantially lower fitted slope for Ru-Co_xPv@C (9.67×10^{-5}) compared to Ru-$Co(OH)_2$ (1.15×10^{-5}) suggests a markedly enhanced hydrogen desorption process (Fig. 5g–i).

3.5 Formation mechanism of local acidic environment

In situ Raman spectroscopy was performed to gain deeper insight into the enhanced catalytic performance of Ru-Co_xPv@C, which is attributed to the formation of a localized acid-like environment (Fig. 6a).[49] For alkaline seawater HER, the Raman spectra of Ru-$Co(OH)_2$ and Ru-Co_xPv@C were recorded as the overpotential increased from 0.02 to 0.10 V. As demonstrated in Fig. 6b–e, in addition to the prominent peaks at 1350 and 1593 cm^{-1}, which correspond to the characteristic D and G bands of carbon, two additional peaks at 1192 and 1543 cm^{-1} were observed in the Ru-Co_xPv@C sample. These peaks are attributed to the vibrational modes of dual Co–Co sites ($\delta_{Co-OH-Co}$) and Ru–Ru sites ($\delta_{Ru-OH-Ru}$) in the Ru-Co_xPv@C sample, respectively. Notably, their intensities progressively increase with rising overpotential, indicating the dynamic evolution of active sites during the HER process.[50] However, Ru-$Co(OH)_2$ exhibits only the $\delta_{Ru-OH-Ru}$ peak during the HER test, suggesting that Ru-Co_xPv@C facilitates the desorption of more strongly adsorbed OH* species. This enhancement is likely attributed to the unique Co sites, which promote OH* desorption, thereby improving the water dissociation kinetics. In contrast, the desorption of Ru–OH remains hindered in the Ru-$Co(OH)_2$ catalyst. Notably, as the overpotential gradually increases, three new Raman peaks are detected at ~2330, ~1885 and ~1750 cm^{-1}, belonging to P–H, Ru–H, and H_3O^+ intermediate species in Ru-Co_xPv@C, respectively, and a weaker peak in the range of 750–900 cm^{-1} ascribed to Ru–H.[25,50–53] The presence of P–H suggests that phosphorus can act as a proton concentrator, storing H^+ and supplying it to the active sites of Ru during the HER. Moreover, the negatively charged Ru atom can also enhance the H^+ adsorption process due to the creation of nanoscale and atomically local electric fields, which subsequently combine with adjacent H_2O molecules to form abundant H_3O^+, creating a local acid-like environment that promotes HSo. Furthermore, in comparison to Ru-Co_xPv@C, Ru-$Co(OH)_2$ exhibits weaker Ru–H at larger applied potential, and hardly shows the H_3O^+ intermediate species peak, and thus has unsatisfactory catalytic performance (Fig. 6f).

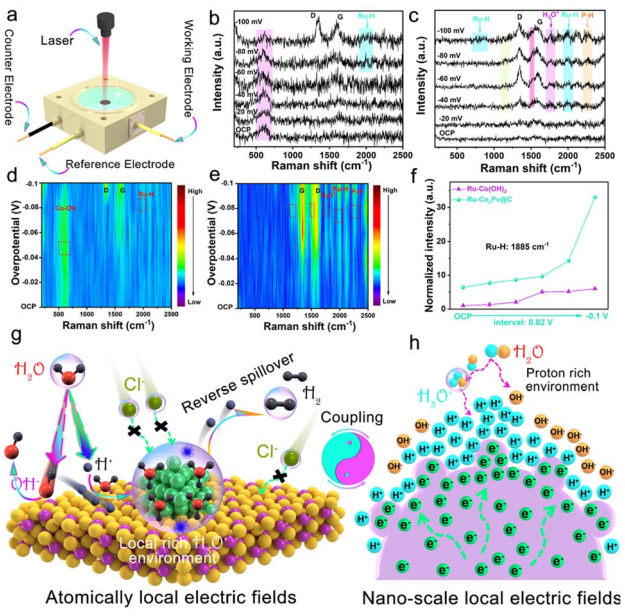

Fig. 6 (a) *In situ* Raman spectroscopy setup. (b and c) *In situ* Raman spectra for Ru-$Co(OH)_2$ and Ru-Co_xPv@C with different operating potentials (*vs.* RHE), and (d and e) 2D contour images of Ru-$Co(OH)_2$ and Ru-Co_xPv@C. (f) Normalized intensity of Ru–H signals for Ru-$Co(OH)_2$ and Ru-Co_xPv@C under different HER potentials. (g) Schematic diagram of the HSo mechanism for Ru-Co_xPv@C. (h) Physicochemical insight into the electron state in the Ru-Co_xPv@C structure.

Based on the above experimental and theoretical results, we propose a HER mechanism for the $Ru^{\delta-}$ NPs in an alkaline seawater solution (Fig. 6). As shown in Fig. 6g, the phosphorus vacancy-rich Co_xPv@C facilitates the water dissociation and transfers abundant electrons to Ru NPs to form negatively charged Ru atoms, thus creating an atomic electric field. Then, the electron-deficient H^+ species spontaneously transfer to Ru and aggregate on the Ru surface, where they subsequently combine with adjacent H_2O molecules to form abundant H_3O^+, creating a local acid-like environment that promotes HSo. Moreover, the carbon layer and the inherent corrosion resistance of Co_xPv@C effectively protect the Ru region from the toxicity and corrosion caused by Cl^- in the alkaline seawater electrolyte, thus achieving excellent HER performance. In addition, the high-curvature nanoparticle structure attracts electrons to the Ru tip region to consolidate this electron-rich state, which is beneficial for proton enrichment at the tip. Specifically, as shown in Fig. 6h, this high-curvature Ru round morphology, resembling a nanopyramid, effectively concentrates electrons at the tip region to induce a high local nanoscale electric field, which is beneficial for the proton enriched environment at the Ru NPs region, indicating that the Ru NPs region with enriched electrons can promote a local acidic proton-rich environment for HSo under alkaline conditions.

4. Conclusions

We propose a cooperative strategy that establishes both nanoscale and atomically local electric fields to generate a high-concentration local acid-like environment for HSo. FEM simulations and related characterizations illustrate that the these local electric fields promote the formation of a significant amount of H_3O^+, creating a local acid-like environment around the surface of the Ru nanoparticles. The small $\Delta\Phi$ of 0.05 eV between Ru and Co_xP is beneficial to the interface HSo. *In situ* Raman spectroscopy confirms that the formed P–H bond acts as a proton "sponge", storing H^+ ions and quickly transferring them to the Ru NPs surface, where they combine with adjacent H_2O molecules to form H_3O^+, thus promoting HSo. Importantly, the carbon layer and the inherent corrosion resistance of Co_x-Pv@C effectively protect the Ru NPs from the toxicity and corrosion caused by Cl^-. Consequently, the Ru-Co_xPv@C catalyst exhibits a small overpotential of 94 mV to achieve η_{10} with a long-term stability for 200 h at this current in alkaline seawater electrolyte.

Data availability

All data that support the findings of this study are included within the article.

Author contributions

Lei Jin: conceptualization, methodology, writing – original draft, data curation, visualization. Zhiyuan Wang: investigation, formal analysis. Hui Xu: methodology, formal analysis, writing – review & editing. Kun Wang: data curation. Xingyue Qian: formal analysis, supervision, writing – review & editing. Haiqun Chen: project administration. Guangyu He: validation, funding acquisition, resources.

Conflicts of interest

The authors declare that they have no known competing financial interests or personal relationships that could have appeared to influence the work reported in this paper.

Acknowledgements

This work was financially supported by the National Natural Science Foundation of China (No. 52472043, 22305025, and 22078028), the Natural Science Foundation of Jiangsu Province (BK20230640), and the China National Petroleum Corporation (CNPC) Innovation Fund (2024DQ02-0310). We also thank the Analysis and Testing Center of Changzhou University for assistance in characterization studies.

Notes and references

1 S. Kim, H. Zhong, Y. Park, F. Loose and P. J. Chirik, Catalytic hydrogenation of a manganese (V) nitride to ammonia, *J. Am. Chem. Soc.*, 2020, **142**, 9518–9524.
2 L. Wang, L. Wang, J. Zhang, X. Liu, H. Wang, W. Zhang, Q. Yang, J. Ma, X. Dong and S. J. Yoo, Selective hydrogenation of CO_2 to ethanol over cobalt catalysts, *Angew. Chem., Int. Ed.*, 2018, **57**, 6104–6108.
3 H. Wang, E. Harkou, A. Constantinou, S. M. Al-Salemc, G. Manos and J. Tang, From photocatalysis to photon-phonon co-driven catalysis for methanol reforming to hydrogen and valuable by-products, *Chem. Soc. Rev.*, 2025, **54**, 2188–2207.
4 X. Chen, D. Menon, X. Wang, M. He, M. R. A. Kiapi, M. Asgari, Y. Lyu, X. Tang, L. L. Keenan and W. Shepard, Flexibility-frustrated porosity for enhanced selective CO_2 adsorption in an ultramicroporous metal-organic framework, *Chem*, 2025, **11**, 102382.
5 H. Jin, J. Xu, H. Liu, H. Shen, H. Yu, M. Jaroniec, Y. Zheng and S.-Z. Qiao, Emerging materials and technologies for electrocatalytic seawater splitting, *Sci. Adv.*, 2023, **9**, eadi7755.
6 X. Zhang, Z. Zuo, C. Liao, F. Jia, C. Cheng and Z. Guo, Strategies for designing advanced transition metal-based electrocatalysts for alkaline water/seawater splitting at ampere-level current densities, *ACS Catal.*, 2024, **14**, 18055–18071.
7 H. Xie, Z. Zhao, T. Liu, Y. Wu, C. Lan, W. Jiang, L. Zhu, Y. Wang, D. Yang and Z. Shao, A membrane-based seawater electrolyser for hydrogen generation, *Nature*, 2022, **612**, 673–678.
8 Y. Liu, Y. Wang, P. Fornasiero, G. Tian, P. Strasser and X. Y. Yang, Long-term durability of seawater electrolysis for hydrogen: From catalysts to systems, *Angew. Chem., Int. Ed.*, 2024, **136**, e202412087.
9 S. Chen, Y. Zhuo, X. Wang, S. Li, J. Lu, D. Liu, H. Pan and Z. Wang, Advances of layered double hydroxide electrocatalysts for high-current-density alkaline water/seawater splitting, *Coord. Chem. Rev.*, 2024, **510**, 215832.
10 L. Jin, H. Xu, K. Wang, Y. Liu, X. Qian, H. Chen and G. He, Modulating built-in electric field via Br induced partial phase transition for robust alkaline freshwater and seawater electrolysis, *Chem. Sci.*, 2025, **16**, 329–337.
11 Z. Chen, M. Yang, Y. Li, W. Gong, J. Wang, T. Liu, C. Zhang, S. Hou, G. Yang and H. Li, Termination-acidity tailoring of molybdenum carbides for alkaline hydrogen evolution reaction, *Nat. Commun.*, 2025, **16**, 418.
12 H. Xu, J. Yuan, G. He and H. Chen, Current and future trends for spinel-type electrocatalysts in electrocatalytic oxygen evolution reaction, *Coord. Chem. Rev.*, 2023, **475**, 214869.
13 B. Huang, J. Yan, Z. Li, L. Chen and J. Shi, Anode-electrolyte interfacial acidity regulation enhances electrocatalytic performances of alcohol oxidations, *Angew. Chem., Int. Ed.*, 2024, **63**, e202409419.
14 W. Shao, Z. Xing, X. Xu, D. Ye, R. Yan, T. Ma, Y. Wang, Z. Zeng, B. Yin and C. Cheng, Bioinspired proton pump on ferroelectric HfO_2-coupled Ir catalysts with bidirectional hydrogen spillover for pH-universal and superior hydrogen production, *J. Am. Chem. Soc.*, 2024, **146**, 27486–27498.
15 Y. Liu, L. Li, L. Wang, N. Li, X. Zhao, Y. Chen, T. Sakthivel and Z. Dai, Janus electronic state of supported iridium

nanoclusters for sustainable alkaline water electrolysis, *Nat. Commun.*, 2024, **15**, 2851.

16 H. Xu, Y. Liu, K. Wang, L. Jin, J. Chen, H. Chen and G. He, High-entropy layered double hydroxides tailor Pt electron state for promoting acidic hydrogen evolution reaction, *J. Colloid Interface Sci.*, 2025, **684**, 566–574.

17 W. Hao, X. Ma, L. Wang, Y. Guo, Q. Bi, J. Fan, H. Li and G. Li, Surface corrosion-resistant and multi-scenario MoNiP electrode for efficient industrial-scale seawater splitting, *Adv. Energy Mater.*, 2024, **15**, 2403009.

18 W. Liu, J. Yu, M. G. Sendeku, T. Li, W. Gao, G. Yang, Y. Kuang and X. Sun, Ferricyanide armed anodes enable stable water oxidation in saturated saline water at 2 A/cm^2, *Angew. Chem., Int. Ed.*, 2023, **135**, e202309882.

19 Z. Li, Y. Yao, S. Sun, J. Liang, S. Hong, H. Zhang, C. Yang, X. Zhang, Z. Cai and J. Li, Carbon oxyanion self-transformation on NiFe oxalates enables long-term ampere-level current density seawater oxidation, *Angew. Chem., Int. Ed.*, 2024, **63**, e202316522.

20 H. Chen, P. Liu, W. Li, W. Xu, Y. Wen, S. Zhang, L. Yi, Y. Dai, X. Chen and S. Dai, Stable seawater electrolysis over 10000 h via chemical fixation of sulfate on NiFeBa-LDH, *Adv. Mater.*, 2024, **36**, 2411302.

21 S. Hou, Y. Xu, Z. Chen, G. Yang, C. Zhu, X. Fan, X. Weng, J. Wang, L. Wang and Y. Cui, Ru single atoms tailoring the acidity of metallic tungsten dioxide for a boosted alkaline hydrogen evolution reaction, *ACS Catal.*, 2024, **14**, 8238–8251.

22 L. Wang, Y. Chen, Y. Liu, Q. Dai, Z. Chen, X. Yang, Y. Luo, Z. Li, B. Yang and M. Zheng, Electron redistribution of Ru Site on MoO_2@$NiMoO_4$ support for efficient ampere-level current density electrolysis of alkaline seawater, *Small*, 2024, **20**, 2311477.

23 L. Song, L. Guo, J. Mao, Z. Li, J. Zhu, J. Lai, J. Chi and L. Wang, Boosting hydrogen adsorption via manipulating the d-band center of ferroferric oxide for anion exchange membrane-based seawater electrolysis, *ACS Catal.*, 2024, **14**, 6981–6991.

24 J. Guo, Y. Zheng, Z. Hu, C. Zheng, J. Mao, K. Du, M. Jaroniec, S.-Z. Qiao and T. Ling, Direct seawater electrolysis by adjusting the local reaction environment of a catalyst, *Nat. Energy*, 2023, **8**, 264–272.

25 H. Tan, B. Tang, Y. Lu, Q. Ji, L. Lv, H. Duan, N. Li, Y. Wang, S. Feng and Z. Li, Engineering a local acid-like environment in alkaline medium for efficient hydrogen evolution reaction, *Nat. Commun.*, 2022, **13**, 2024.

26 H. Hu, Z. Zhang, L. Liu, X. Che, J. Wang, Y. Zhu, J. P. Attfield and M. Yang, Efficient and durable seawater electrolysis with a V_2O_3-protected catalyst, *Sci. Adv.*, 2024, **10**, eadn7012.

27 D. Bao, L. Huang, Y. Gao, K. Davey, Y. Zheng and S.-Z. Qiao, Dynamic creation of a local acid-like environment for hydrogen evolution reaction in natural seawater, *J. Am. Chem. Soc.*, 2024, **146**, 34711–34719.

28 H. Chen, Y.-Q. Wang, R. Ding, Z.-W. Zeng, B.-W. Liu, F.-R. Zeng, Y.-Z. Wang and H.-B. Zhao, Satellite-like shielding for dual single-atom catalysis, boosting ampere-level alkaline seawater splitting, *Matter*, 2024, **7**, 3189–3204.

29 Z. Chen, W. Gong, J. Wang, S. Hou, G. Yang, C. Zhu, X. Fan, Y. Li, R. Gao and Y. Cui, Metallic W/WO_2 solid-acid catalyst boosts hydrogen evolution reaction in alkaline electrolyte, *Nat. Commun.*, 2023, **14**, 5363.

30 T. Li, B. Wang, Y. Cao, Z. Liu, S. Wang, Q. Zhang, J. Sun and G. Zhou, Energy-saving hydrogen production by seawater electrolysis coupling tip-enhanced electric field promoted electrocatalytic sulfion oxidation, *Nat. Commun.*, 2024, **15**, 6173.

31 D. Qi, Y. Wang, X. Xu, X. Jiang, M. Ahmad, Z. Chao, Z. Yu, M. Lian, Y. Wang and Z. Zhang, Promoting active species generation by sculpting Co_3S_4/$Co(OH)_2$ nanotubes with rich sulfide/hydroxide interfaces for efficient oxygen evolution reaction, *J. Electroanal. Chem.*, 2023, **943**, 117619.

32 G. Zhou, M. Li, Y. Li, H. Dong, D. Sun, X. Liu, L. Xu, Z. Tian and Y. Tang, Regulating the electronic structure of CoP nanosheets by O incorporation for high-efficiency electrochemical overall water splitting, *Adv. Funct. Mater.*, 2020, **30**, 1905252.

33 X. Liu, W. Yan, J. Song, H. Song, W. Chen, Y. Zhang and Y. Chen, Kirkendall effect induced the formation of hollow Co_2P in Co-NC for ORR, OER, HER and flexible Zn-Air battery, *Chem. Eng. J.*, 2024, **492**, 152301.

34 H. Xu, L. Jin, K. Wang, L. Yang, G. He and H. Chen, Carbon nanocages confined multicomponent phosphide heterostructures for boosting oxygen evolution reaction in alkaline water and seawater, *Int. J. Hydrogen Energy*, 2023, **48**, 38324–38334.

35 E. Safaralizadeh, S. J. Darzi, A. R. Mahjoub and R. Abazari, Visible light-induced degradation of phenolic compounds by Sudan black dye sensitized TiO_2 nanoparticles as an advanced photocatalytic material, *Res. Chem. Intermed.*, 2017, **43**, 1197–1209.

36 W. Zhu, W. Hu, Y. Wei, Y. Zhang, K. Pan, S. Zhang, X. Hang, M. Zheng and H. Pang, Core-shell Co-Co_xP nanoparticle-embedded N-doped carbon nanowhiskers hollow sphere for efficient oxygen evolution electrocatalysis, *Adv. Funct. Mater.*, 2024, **34**, 2409390.

37 Y. Deng, L. Tan, T. Wang, S. Bai, J. Sun, J. Guo, T. Li, G. Liu and S. Zhang, Fast synthesis of low Ru doped CoO_x/CeO_2 nanosheet arrays with abundant heterointerfaces for highly efficient overall water splitting, *Int. J. Hydrogen Energy*, 2024, **88**, 199–208.

38 T. Liu, P. Li, N. Yao, G. Cheng, S. Chen, W. Luo and Y. Yin, CoP-doped MOF-based electrocatalyst for pH-universal hydrogen evolution reaction, *Angew. Chem., Int. Ed.*, 2019, **131**, 4727–4732.

39 Q. Wang, Y. Gong, X. Zi, L. Gan, E. Pensa, Y. Liu, Y. Xiao, H. Li, K. Liu and J. Fu, Coupling nano and atomic electric field confinement for robust alkaline oxygen evolution, *Angew. Chem., Int. Ed.*, 2024, **136**, e202405438.

40 H. Xu, J. Chen, Y. Liu, L. Jin, K. Wang, H. Chen and G. He, Weakening the resistance of built-in electric fields through phase-engineered work function for enhanced electrocatalytic hydrogen evolution reaction, *Fuel*, 2025, **400**, 135763.

41 J. Li, J. Hu, M. Zhang, W. Gou, S. Zhang, Z. Chen, Y. Qu and Y. Ma, A fundamental viewpoint on the hydrogen spillover phenomenon of electrocatalytic hydrogen evolution, *Nat. Commun.*, 2021, **12**, 3502.

42 X. Liu, X. Wang, K. Li, J. Tang, J. Zhu, J. Chi, J. Lai and L. Wang, Diluting the resistance of built-in electric fields in oxygen vacancy-enriched Ru/$NiMoO_{4-x}$ for enhanced hydrogen spillover in alkaline seawater splitting, *Angew. Chem., Int. Ed.*, 2024, **63**, e202316319.

43 Y. Song, M. Sun, S. Zhang, X. Zhang, P. Yi, J. Liu, B. Huang, M. Huang and L. Zhang, Alleviating the work function of vein-like Co_xP by Cr doping for enhanced seawater electrolysis, *Adv. Funct. Mater.*, 2023, **33**, 2214081.

44 B. Wang, M. Lu, D. Chen, Q. Zhang, W. Wang, Y. Kang, Z. Fang, G. Pang and S. Feng, Ni_xFe_yN@C microsheet arrays on Ni foam as an efficient and durable electrocatalyst for electrolytic splitting of alkaline seawater, *J. Mater. Chem. A*, 2021, **9**, 13562–13569.

45 X. Xu, Y. Lu, J. Shi, X. Hao, Z. Ma, K. Yang, T. Zhang, C. Li, D. Zhang and X. Huang, Corrosion-resistant cobalt phosphide electrocatalysts for salinity tolerance hydrogen evolution, *Nat. Commun.*, 2023, **14**, 7708.

46 Y. Chen, Y. Liu, L. Li, T. Sakthivel, Z. Guo and Z. Dai, Intensifying the supported ruthenium metallic bond to boost the interfacial hydrogen spillover toward pH-universal hydrogen evolution catalysis, *Adv. Funct. Mater.*, 2024, **34**, 2401452.

47 S. Pan, C. Li, T. Xiong, Y. Xie, F. Luo and Z. Yang, A Hydrogen spillover in MoO_xRh hierarchical nanosheets boosts alkaline HER catalytic activity, *Appl. Catal., B*, 2024, **341**, 123275.

48 R. Rajalakshmi, G. Srividhya, C. Viswanathan and N. Ponpandian, Hydrogen spillover effect-harnessing hydrogen evolution reaction from diverse carbon-based supports with a tungsten oxide catalyst, *J. Mater. Chem. A*, 2023, **11**, 15889–15905.

49 S. Zhao, Y. Wang, Y. Hao, L. Yin, C. H. Kuo, H. Y. Chen, L. Li and S. Peng, Lewis acid driving asymmetric interfacial electron distribution to stabilize active species for efficient neutral water oxidation, *Adv. Mater.*, 2024, **36**, 2308925.

50 H. Ren, Z. Zhang, Z. Geng, Z. Wang, F. Shen, X. Liang, Z. Cai, Y. Wang, D. Cheng and Y. Cao, Gradient OH desorption facilitating alkaline hydrogen evolution over ultrafine quinary nanoalloy, *Adv. Energy Mater.*, 2024, **14**, 2400777.

51 Y. Yuan, Y. Li, G. Fang, G. Liu, C. Pei, X. Li, H. Zheng, K. Yang and L. Wang, Stoichiometric evolutions of PH_3 under high pressure: implication for high-Tc superconducting hydrides, *Natl. Sci. Rev.*, 2019, **6**, 524–531.

52 L. Hou, C. Li, H. Jang, M. G. Kim, J. Z. Jiang, J. Cho, S. Liu and X. Liu, Rationally designed Mo/Ru-based multi-site heterogeneous electrocatalyst for accelerated alkaline hydrogen evolution reaction, *Adv. Mater.*, 2024, **36**, 2410039.

53 H. Zhang, W. Liu, Z. Li, L. Qiao, K. Chi, X. Guo, D. Cao and D. Cheng, Constructing CoP/Ni_2P heterostructure confined Ru sub-nanoclusters for enhanced water splitting in wide pH conditions, *Adv. Sci.*, 2024, **11**, 2401398.